Dependence of pressure in a compressed condensed matter on parameters of high-power laser pulses

A.I. Lebo, I.G. Lebo, D. Batani

Abstract. **Based on analysis of two-dimensional numerical calculations and experiments performed on the PALS setup, the similarity relations are obtained for determining pressure in a condensed matter irradiated by a short laser pulse of intensity $5 \times 10^{13} - 5 \times 10^{14}$ W cm^{-2}.**

1. Introduction

Under irradiation of a condensed matter by high-power pulses, a high-temperature plasma propagating toward the laser beam is produced and intense shock waves propagate deep in a nonevaporated matter. A pressure jump at the front of these waves can achieve tens (in some cases, even hundreds) of millions of atmospheres (megabars). The behaviour of matter under such extremal conditions is of interest for researchers studying the problems of nuclear fusion and astrophysics, and involved in some applied investigations. Therefore, the question of what pressures are produced in a condensed matter at different radiation parameters and different materials of a target is of current interest. The direct measurement of such pressures in compressed materials is a challenging experimental problem. In this connection it is useful to perform numerical calculations and, by comparing them with experimental data, to obtain similarity relations (scalings) for determining these pressures from the known data on parameters of radiation and targets.

The thermodynamic parameters of compressed laser-induced plasmas have been determined in numerous experimental and theoretical studies preformed in our country and abroad (see, for example, [1 – 8]). The relations obtained in these studies describe qualitatively the behaviour of materials irradiated by high-power laser pulses. Nevertheless, the analysis of concrete experiments requires

A.I. Lebo Department of Physics, M.V. Lomonosov Moscow State University, Vorob'evy gory, 119992 Moscow, Russia;
I.G. Lebo Moscow State Institute of Radio-Engineering, Electronics and Automation (Technical University), prosp. Vernadskogo 78, 119454 Moscow, Russia; e-mail: lebo@mirea.ru;
D. Batani Dipartimento di Fisica 'G. Occhialini', Università di Milano Bicocca, Piazza della Scienza 3, 20126 Milano, Italy

additional investigations to take into account different effects such as the nonstationarity of a plasma corona, the influence of geometrical factors, ionisation, recombination, etc. Numerical calculations allow one to take into account these effects and to obtain general expressions, which can be used to analyse available experimental data and plan future experiments.

In this paper, we present the results of two-dimensional numerical simulations of experiments performed on the PALS setup (Prague Asterix Laser System) at the Physics Institute, Czech Academy of Sciences [9], derive the similarity relation based on two-dimensional numerical calculations, and discuss the results obtained.

2. Brief description of the program

Computational experiments were performed by applying the Atlant software program, which uses the two-dimensional Lagrange cylindrical geometry (coordinates r and z). The basic equations, which were solved by the finite difference methods, have the form

$$\frac{\mathrm{d}\rho}{\mathrm{d}t} = -\rho\nabla\boldsymbol{v},$$

$$\rho\,\frac{\mathrm{d}\boldsymbol{v}}{\mathrm{d}t} = -\nabla(Z_i p_e + p_i + p_r),$$

$$Z_i\rho\,\frac{\mathrm{d}E_e}{\mathrm{d}t} = -Z_i p_e\nabla\boldsymbol{v} + \nabla(\kappa_e\nabla T_e)$$

$$- Q_{ei} - Q_{er} - R_{rad}(\rho, T_e) + \nabla\boldsymbol{q},$$

$$\rho\,\frac{\mathrm{d}E_i}{\mathrm{d}t} = -p_i\nabla\boldsymbol{v} + \nabla(\kappa_i\nabla T_i) + Q_{ei},$$

$$\rho\,\frac{\mathrm{d}E_r}{\mathrm{d}t} = -p_r\nabla\boldsymbol{v} + \nabla(\kappa_r\nabla T_r) + Q_{er},$$

$$\left(\frac{\boldsymbol{q}}{|\boldsymbol{q}|}\nabla\right)\boldsymbol{q} = k(\rho, T_e)\boldsymbol{q},$$

where

$$Q_{ei} = Q_{0ei}\,\frac{T_e - T_i}{T_e^{3/2}}\,Z_i\rho^2; \quad Q_{er} = Q_{0er}\,\frac{T_e - T_r}{T_e^{1/2}}\,Z_i\rho^2;$$

$$p_e = p_e(\rho, T_e); \quad p_i = p_i(\rho, T_i); \quad p_r = p_r(\rho, T_r);$$

$$E_e = E_e(\rho, T_e); \quad E_i = E_i(\rho, T_i); \quad E_r = E_r(\rho, T_r);$$

ρ is the density; $\boldsymbol{v}$ is velocity vector; $\boldsymbol{q}$ is the laser radiation flux; κ_e, κ_i, and κ_r are the electron, ion, and radiative heat conductivities, respectively; k is the absorption coefficient; E_e E_i, and E_r are the specific internal energies of electrons, ions, and photons; R_{rad} is the reemission energy loss; p_e, p_i, p_r and T_e, T_i, T_r are the electron, ion, and radiative components of pressure and temperature, respectively; E_e and p_e are normalised to the unity of the average charge Z_i in a Lagrangian cell; Q_{ei} and Q_{er} are the rates of energy exchange between electrons and ions and between electrons and photons, respectively. The physicomathematical model and the methods of solving the equations written above are described in detail in monograph [10].

The Atlant program uses three models for the equation of state of matter: the ideal gas model, the QEOS (quotidian equations of states) model [11], and the model developed at Lebedev Physics Institute [10, 12], which is based on the theory described in the monograph of Zel'dovich and Raizer [13] (we will call this model the ZRI model, i.e. the Zel'dovich – Raizer model taking the ionisation kinetics into account).

The propagation of laser radiation in plasmas is calculated in the geometric optics approximation. The laser beam is divided into discrete rays (ray tracing), the energy being released along the ray path in accordance with the inversely braking absorption mechanism. This approach was first used for calculations of laser targets in [14] and applied to the Atlant program in [15]. Because the laser radiation energy reflected from plasma was not measured in our experiments, we assumed in calculations that the rays propagated strictly parallel to the z axis and energy was absorbed in the first Lagrange cell in which the electron concentration exceeded the critical value. The calculations neglected radiation energy transfer (the two-temperature model) because we considered materials consisting of atoms with small nuclear charges (aluminium and polyethylene).

3. Analysis of experimental data by using two-dimensional calculations

In experiments performed earlier, profiled aluminium targets in the form of a 'step' covered by a thin polymer layer were irradiated by the 0.438-μm third harmonic of the PALS iodine laser. The laser pulse energy was varied

between 50 and 250 J. Laser pulses had the Gaussian shape with the FWHM equal to 0.4 ns.

The aluminium target was made in the form of a 'step' consisting of the upper (with respect to incident radiation) layer of thickness $d_1 = 8$ μm covered with a polyethylene layer of thickness $d_{peth} = 2$ μm (these two layers form the 'base' of the target) and the lower layer of thickness $d_2 = 8.5$ μm. The accuracy of measuring the shock wave velocity was $\pm 5\%$. In experiments, the laser pulse energy introduced into the interaction chamber was measured. Because the accuracy of focusing laser radiation on a target was measured only before each series of shots, the estimates of the laser radiation intensity on the target could have a scatter within $\pm 10\%$. These experiments and obtained results are described in more detail in [9].

The laser pulse shape was specified in calculations by an isosceles triangle with apexes corresponding to the instants of time 0, 0.4, and 0.8 ns. To prevent the destruction of a Lagrangian network, the step profile of the target was smoothed by half the sinusoid with the half-period $\lambda_p = 20$ μm, as shown in Fig. 1. The transverse radius of the calculation region was $R_0 = 200$ μm. Calculations were performed by varying the radiation power, assuming that the radiation intensity in the beam cross section was constant along the beam radius. For the specified absorbed energy E_{las}^{abs} and a triangular pulse, the maximum radiation intensity is $I_{max} = 2E_{las}^{abs}/(\pi R_f^2 \tau_{las})$, where R_f is the focal spot radius and τ_{las} is the pulse duration.

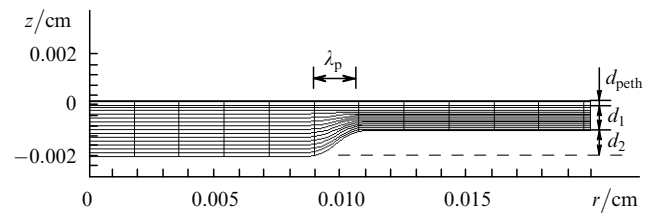**Figure 1.** Initial Lagrangian network used in calculations ($d_{peth} = 2$ μm, $d_1 = 8$ μm, $d_2 = 8.5$ μm, $\lambda_p = 20$ μm). Laser radiation is incident from above.

We present below the results of calculations performed for $R_f = R_0 = 200$ μm. Figure 2 shows the spatial distributions of the plasma density in a target calculated for the laser pulse energy equal to 100 J. The plasma density distribution presented in Fig. 2a corresponds to $t = 0.35$ ns [a calculated shock wave arrives at the external boundary of the target base (the first boundary) at the
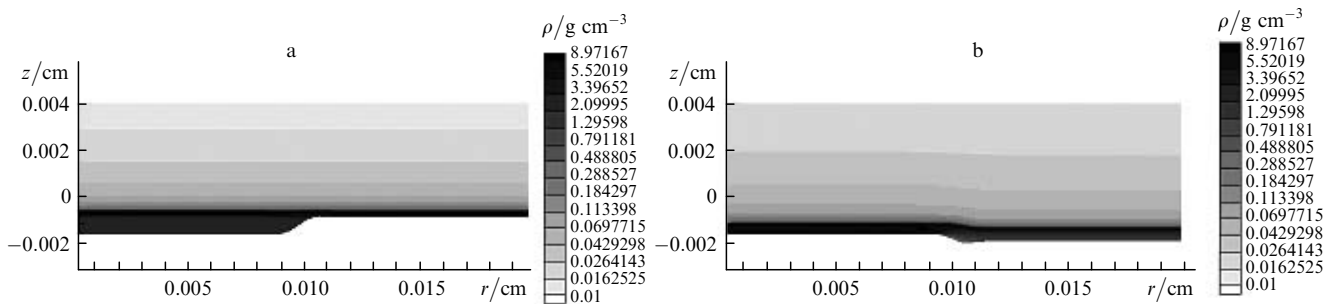

Figure 2. Spatial distribution of the plasma density in a target at instants $t = 0.35$ (a) and 0.55 ns (b); $E_{las}^{abs} = 100$ J. Laser radiation is incident in the direction opposite to the z axis direction.

instant $t_1 = 0.3257$ ns]. The plasma density distribution shown in Fig. 2b corresponds to $t = 0.55$ ns [the instant $t_2 = 0.555$ ns when the shock wave arrives at the top of the step (the second boundary)]. By knowing these two instants and the layer thickness, we can estimate the shock-wave velocity V_{sw} and then, by using the Hugoniot relation [13], to calculate other parameters behind the wave front. In our computational experiment, $V_{sw} = d_2/(t_2 - t_1) = 37.07$ km s^{-1}.

Because the expansion velocity of matter after the arrival of the shock wave exceeds that of the shock wave in condensed matter, the step profiles in Figs 2a and b are different.

To estimate the influence of the transverse motion of the plasma on the shock-wave velocity in the lower part of the target, we performed quasi-one-dimensional calculations by using the Atlant program.* The target consisted of two regions: the external polyethylene layer with the initial thickness of 2 μm ($0 < z < 2$ μm) and the aluminium layer

---

* A one-dimensional problem was solved by using the Atlant program, but with two cells in the transverse direction which reduced the processor calculation time by an order of magnitude
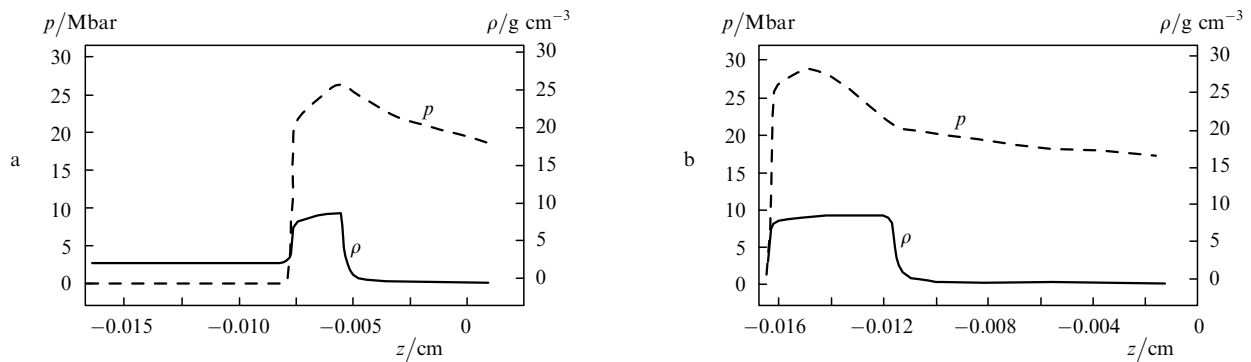
of thickness $d = 16.5$ μm (-16.5 μm $< z < 0$). The shock wave propagated through the upper layer by the instant $t_1 = 0.3226$ ns and achieved the external boundary of the lower layer by the instant $t_2 = 0.5576$ ns. These results are very close to those obtained for a profiled target. Figure 3 shows the density and pressure profiles at different instants. It follows from our calculations that the average velocity of the shock wave, as in the two-dimensional case, is 37.1 km s^{-1}.

Figure 4 presents the density and pressure profiles along the z axis for $r = 0$ and 197.5 μm, obtained in two-dimensional calculations for energy $E_{las}^{abs} = 68$ J. In this case, the shock wave reached the first boundary at the instant $t = 0.37$ ns and the second – at the instant $t = 0.619$ ns. Figures 4a, b show the pressure and density profiles at the instant $t_1 = 0.4$ ns and Figure 4c, d – at the instant $t_2 = 0.65$ ns.

The distance propagated by the shock wave in the condensed matter during the pulse action is considerably smaller than the transverse size of the calculation region and depends only on the intensity for fixed parameters of the laser pulse. Because of this, further calculations were performed for targets with transverse dimensions reduced

Figure 3. Profiles of density ρ and pressure p at instants $t_1 = 0.3226$ ns (the shock-wave front reached $z = -8$ μm) (a) and $t_2 = 0.5576$ ns (the shock-wave front reached $z = -16.5$ μm) (b); $E_{las}^{abs} = 100$ J.
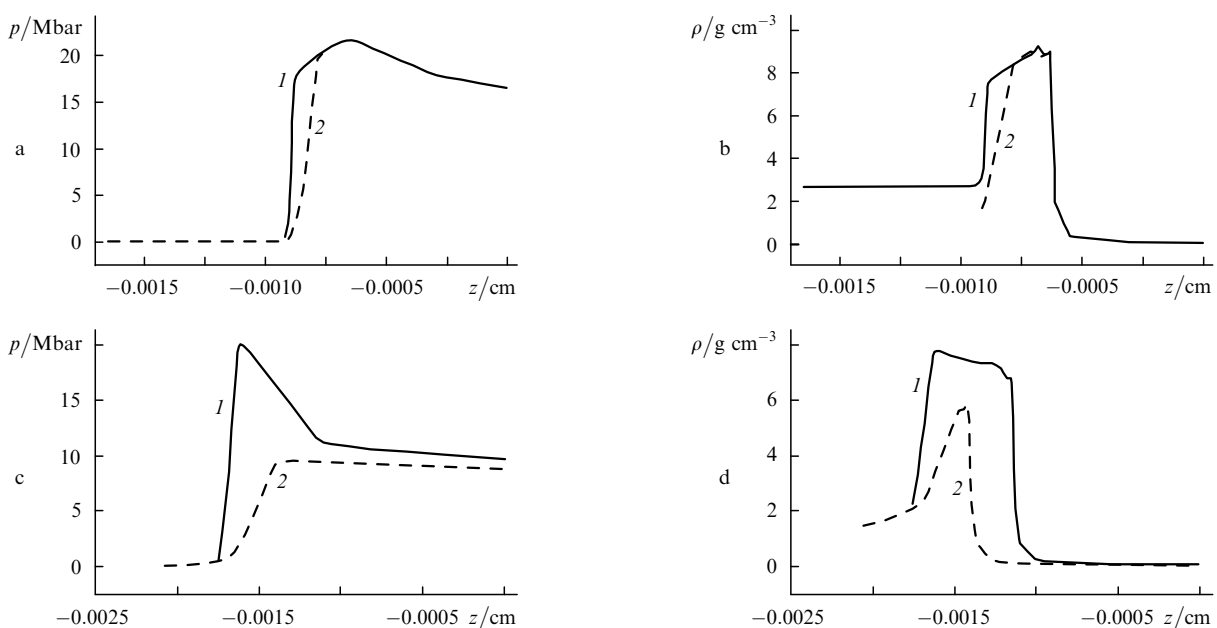

Figure 4. Distributions of pressure p (a, c) and density ρ (b, d) along the z axis near it for $r = 0$ (*1*) and near the target edge for $r = 197.5$ μm (*2*), obtained in two-dimensional calculations at instants $t_1 = 0.4$ ns (a, b) and $t_2 = 0.654$ ns (c, d); $E_{las}^{abs} = 68$ J.
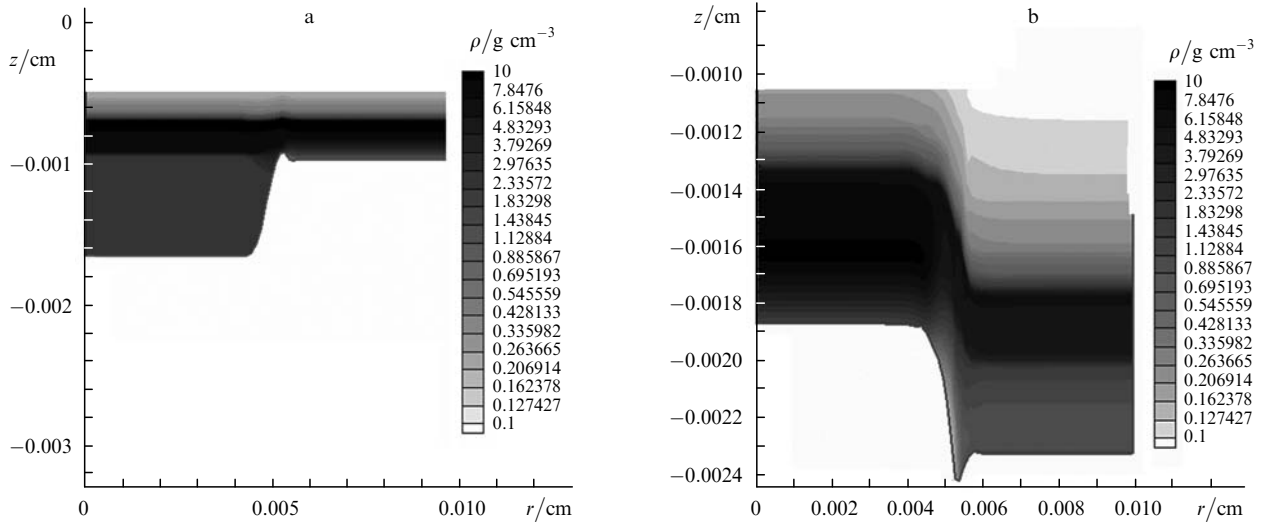
Figure 5. Two-dimensional calculations of the density distributions at instants when the shock wave reached the first boundary ($t_1 = 0.274$ ns) (a) and second boundary ($t_2 = 0.467$ ns) (b).

by half (which reduced the processor time and gave descriptive results). Figure 5 demonstrates the propagation of the shock wave in matter with velocity $V_{sw} = 44$ km s^{-1} for $I_{max} = 4 \times 10^{14}$ W cm^{-2}.

Figure 6 presents the calculated dependences of the average velocities V_{sw} of shock waves on I_{max} and experimental dependences obtained in [9]. One can see that calculated dependences lie on average somewhat higher than experimental ones. This is explained by the fact that in experiments only the energy of radiation entering the chamber was measured, while the energy of reflected and refracted radiation was not detected. Also, the possible influence of plasma reemission was neglected. In our opinion, these losses were approximately 30 %. One can see from Fig. 6 that, if these losses are taken into account, the calculated curve well reproduces the experimental data.
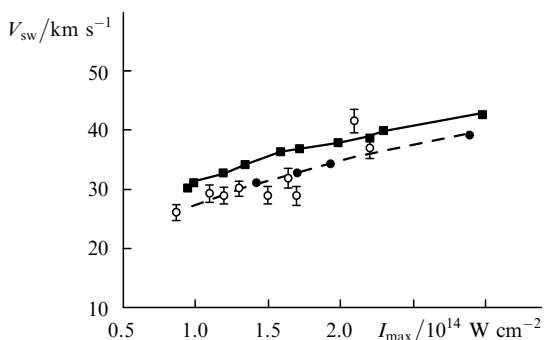

Figure 6. Dependences of the average shock wave velocity V_{sw} on the intensity I_{max}, calculated by neglecting (■) and taking into account (●) energy losses, and experimental data from [9] (○).

The second series of calculations was performed in the quasi-one-dimensional approximation. Based on these calculations, we obtained the similarity relation for describing the dependence of the maximum pressure p_{max} in a compressed material on the intensity I_{max}, wavelength λ, and laser pulse duration τ_{las}. Calculations were performed for aluminium targets of thickness $d = 20 - 60$ µm without polymer coatings and profiling.

Figure 7a shows the dependence of the maximum pressure p_{max} in a condensed matter at the instant $t = 0.4$ ns on the maximum intensity I_{max} of the 0.438-µm third harmonic pulse from an iodine laser. Figure 7b presents the dependence of the maximum pressure p_{max} in a condensed matter at the same instant on the radiation wavelength (0.438, 0.657, and 1.314 µm) for $I_{max} = 1.99 \times 10^{14}$ W cm^{-2}. Note that pressure p_{max} changes both in space and time. Moreover, the ablation pressure, which produces compression and shock waves, changes in time. We will discuss these questions below.
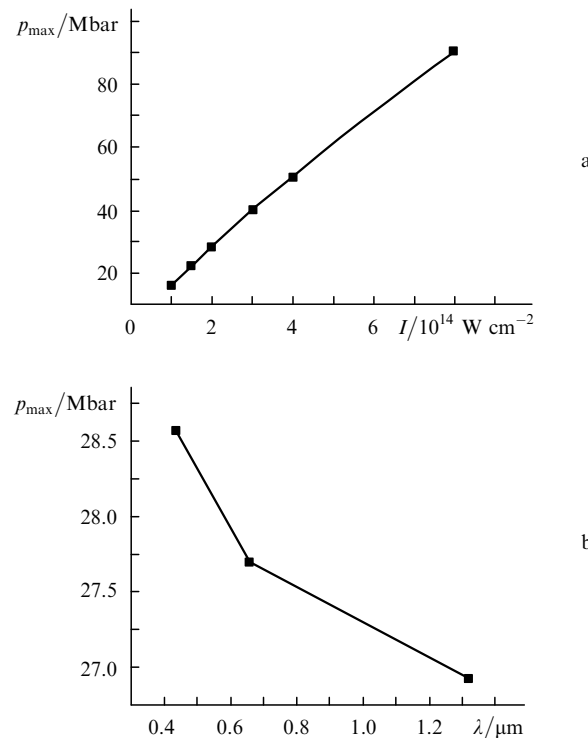

Figure 7. Dependences of the maximum pressure p_{max} at the instat $t = 0.4$ ns on the intensity I_{max} ($\lambda = 0.438$ µm) (a) and laser wavelength ($I_{max} = 1.99 \times 10^{14}$ W cm^{-2}) (b).

Earlier, the results of QEOS calculations were presented. We mentioned above that the program can be used for different models of the equation of state of matter such as the ideal gas models taking into account or neglecting the ionisation kinetics, the ZRI model, and the QEOS model. The ZRI model is noticeably simpler (regarding the volume of operators in the program) and more descriptive, while the QEOS model is widely used in foreign programs. According to the ZRI model, the average charge Z_i of ions, their pressure p_i, and the pressure p_e of electrons are calculated in each Lagrangian cell:

$$\frac{dZ_i}{dt} = Z_i(\varphi_i - \varphi_r - \varphi_{fr}),$$

$$p_i = p_{ti} + p_{el},$$

$$p_e = Z_i n_i T_e,$$

where $p_{ti} = n_i T_i$;

$$p_{el} = \rho_0 C_s^2 \begin{cases} (\rho/\rho_0)^\beta - 1, & \rho/\rho_0 \geqslant 0, \\ 0, & \rho/\rho_0 < 0; \end{cases}$$

$\rho = m_i n_i$; p_{ti} and p_{el} are the thermal and elastic pressure of ions; m_i and n_i are the mass and concentration of ions; φ_i, φ_r, and φ_{fr} are the rates of three-particle ionisation, three-particle recombination, and photorecombination, respectively; ρ_0 and C_s are the initial density and sound speed in a

condensed material under normal conditions; and $\beta \approx 3 - 4$ is the exponent describing the elastic properties of the material.

Another advantage of the ZRI model is that it can describe the expanding plasma in the nonequilibrium ionisation state (the so-called ion annealing effect).

Figure 8 shows pressure distributions for a shock-wave propagating along the z axis in a condensed layer calculated at different instants by using the QEOS (a) and ZRI (b) models. The calculations were performed for the maximum intensity $I_{max} = 1.99 \times 10^{14}$ W cm^{-2}, the laser radiation wavelength $\lambda = 0.438$ μm, and the initial thickness of an aluminium layer $d = 60$ μm. For the convenience of comparison (if the shock-wave velocities would be different in different models), we used the mass coordinates $X_2 = \sum_{j=2}^{n} \Delta M_{2j}$, where ΔM_{2j} are masses of Lagrangian cells bordering the z axis and n is the number of cells corresponding to the coordinate X_2.

One can see that the velocities and amplitudes of shock wave in both cases are close. Thus, the maximum pressure at the instant $t = 0.8$ ns for the QEOS model is 23.5 Mbar ($X_2 = 0.52 \times 10^{-6}$ g) and 22.0 Mbar ($X_2 = 0.51 \times 10^{-6}$ g) for the ZRI model. Pressure jumps behind the shock-wave front in both models also have close amplitudes. The maximum discrepancy was observed for temperatures and average ions charges. Figure 9 presents the distributions of ion charges along the target axis for the two models.

We present below tables of calculations performed by using different models. These results are compared with the approximate formula
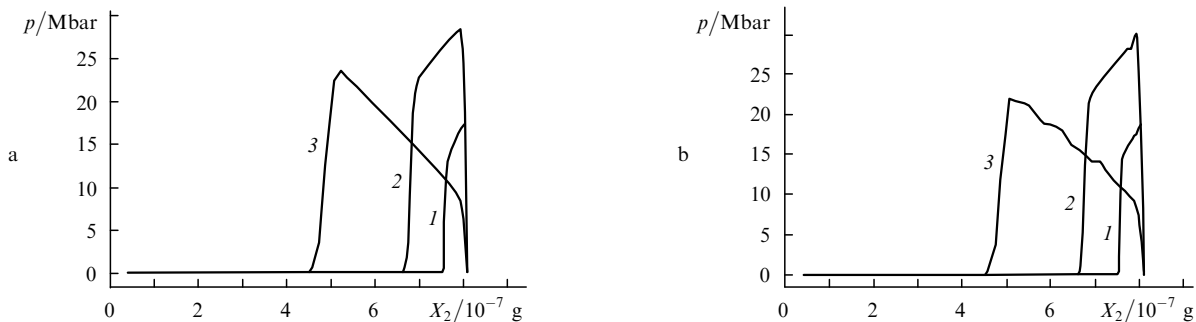

Figure 8. Distributions of pressure p as functions of mass coordinates at instants $t_1 = 0.2$ (1), 0.4 (2), and 0.8 ns (3) for the QEOS (a) and ZRI (b) models.
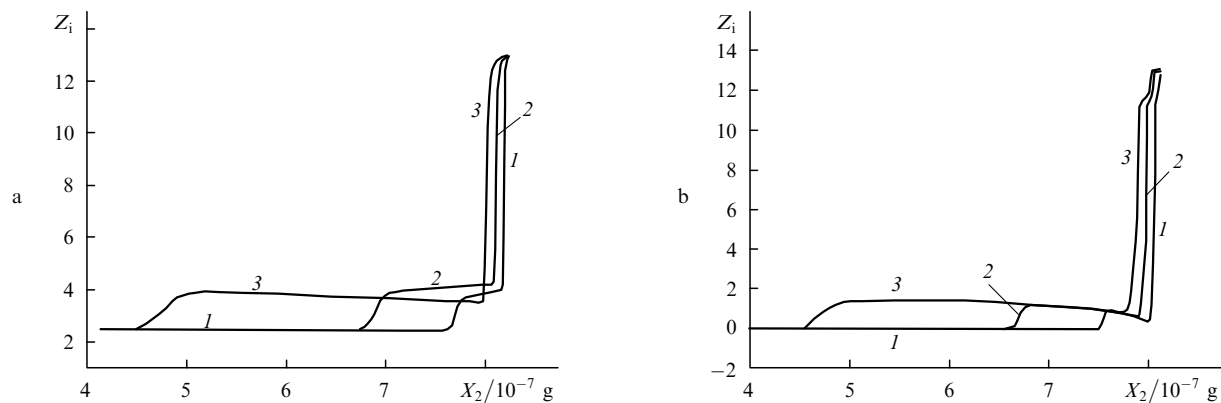

Figure 9. Distributions of average ion charges along the target axis at instants $t = 0.2$ (1), 0.4 (2), and 0.8 ns (3) for the QEOS (a) and ZRI (b) models.

$$p_s^{max} = 28.56 \left(\frac{I_{max}}{1.99 \times 10^{14} \text{ W cm}^{-2}} \right)^{0.83}$$

$$\times \left(\frac{\lambda}{0.438 \text{ }\mu\text{m}} \right)^{-0.056} \tag{1}$$

obtained in our paper, where p_s^{max} is expressed in megabars. Note that the two models give close results, and therefore it is impossible to prefer any of them. Note only that the ZRI model is simpler.

Table 1 presents maximum pressures at the instant 0.4 ns for $\lambda = 0.438$ μm. Calculations were performed for different maximum intensities and fixed laser radiation parameters. One can see that the pressure (and velocity) of the shock wave in the ideal gas model are overstated. This is mainly explained by the fact that this model neglects ionisation losses.

Table 1.

$I_{max}/10^{14}$ W cm^{-2}	$p_{IG}^{max}/$ Mbar	$p_{QEOS}^{max}/$ Mbar	$p_{ZRI}^{max}/$ Mbar	$p_s^{max}/$ Mbar
0.995	24.0	16.06	15.8	16.06
1.49	28.2	22.5	23.8	23.34
1.99	35.4	28.56	30.5	28.56
2.985	49.6	39.98	39.1	39.98
3.98	62.3	50.76	46.5	50.77
7.96	110	90.25	94.2	90.25

N o t e : p_{IG}^{max}, p_{QEOS}^{max}, and p_{ZRI}^{max} are pressures obtained in the ideal gas model with the constant ion charge Z_i, the QEOS and ZRI models, respectively; p_s^{max} are pressures estimated from (1).

Table 2 presents maximum pressures in a condensed material for different laser wavelengths and $I_{max} = 1.99 \times 10^{14}$ W cm^{-2} at the instant $t = 0.4$ ns.

Table 2.

λ/μm	$p_{cal}^{max}/$Mbar	$p_s^{max}/$Mbar
0.438	28.56	28.56
0.655	27.72	27.99
0.876	27.35	27.58
1.31	26.85	27.03

N o t e : p_{cal}^{max} calculated pressures; p_s^{max} pressures estimated from (1).

We also studied the dependence of the maximum pressure on the pulse duration. For this purpose, we performed calculations for a triangular pulse of duration 8 ns (the maximum pulse intensity corresponded to the time $t = 4$ ns). The range of intensities I_{max} was $10^{13} - 5 \times 10^{14}$ W cm^{-2} ($\lambda = 0.438$ μm) and the aluminium layer thickness was $d = 200$ μm. Table 3 presents the results of numerical calculations for 0.8-ns and 8-ns pulses. Pressures p_s^{max} were calculated by the approximate formula

$$p_s^{max} = 28.56 \left(\frac{I}{1.99 \times 10^{14} \text{ W cm}^{-2}} \right)^{0.83}$$

$$\times \left(\frac{\lambda}{0.438 \text{ }\mu\text{m}} \right)^{-0.056} \left(\frac{\tau_{las}}{0.8 \text{ ns}} \right)^{-0.137} \tag{2}$$

Table 3.

$I_{max}/10^{14}$ W cm^{-2}	$p_{max}/$Mbar		$p_s^{max}/$Mbar	
	$\tau_{las} = 0.8$ ns	$\tau_{las} = 8$ ns	$\tau_{las} = 0.8$ ns	$\tau_{las} = 8$ ns
0.2	–	3.234	4.24	3.09
1.49	22.5	16.37	22.46	16.38
1.99	28.56	20.83	28.56	20.83
3.98	50.76	36.38	50.77	37.03

obtained in these calculations, where p_s^{max} is expressed in megabars.

Note that the maximum pressure decreased with increasing pulse duration. We will discuss these results in the next section.

The calculations considered above were performed for aluminium targets. In general, the model used in the Atlant model can be applied for any materials consisting of atoms with a small atomic number A and small nuclear charge Z, i.e. with a small ion charge. In this case, radiant energy transfer can be neglected. To generalise similarity relation (2), we performed calculations for beryllium ($Z = 4$, $A = 9$), graphite ($Z = 6$, $A = 12$), silicon ($Z = 14$, $A = 28$), and copper ($Z = 29$, $A = 64$) for $I_{max} = 1.99 \times 10^{14}$ W cm^{-2} and $\lambda = 0.438$ μm. Based on these calculations, relation (2) was supplemented:

$$p_s^{max} = 28.56 \left(\frac{I_{max}}{1.99 \times 10^{14} \text{ W cm}^{-2}} \right)^{0.83}$$

$$\times \left(\frac{\lambda}{0.438 \text{ }\mu\text{m}} \right)^{-0.056} \left(\frac{\tau_{las}}{0.8 \text{ ns}} \right)^{-0.137} \left(\frac{Z}{13} \right)^{-0.11}, \tag{3}$$

where p_s^{max} is expressed in megabars.

The pressure p_s^{max} behind the front of the shock wave and its velocity V_{sw} are related by the Hugoniot formula

$$V_{sw}^2 = \frac{\gamma + 1}{2} \left(\frac{p_s^{max}}{\rho_0} + \frac{\gamma - 1}{\gamma + 1} \frac{p_0}{\rho_0} \right), \tag{4}$$

where p_0 and ρ_0 are the initial pressure and density and γ is the adiabatic index. Thus, expression (3) can be used to estimate the shock-wave velocity. Note that the radiation intensity changes during irradiation of the target. Moreover, even for the constant laser radiation intensity, pressure will change due to the formation of a plasma corona. Figure 10 presents the results of calculations for a rectangular laser pulse of intensity 1.99×10^{14} W cm^{-2}.
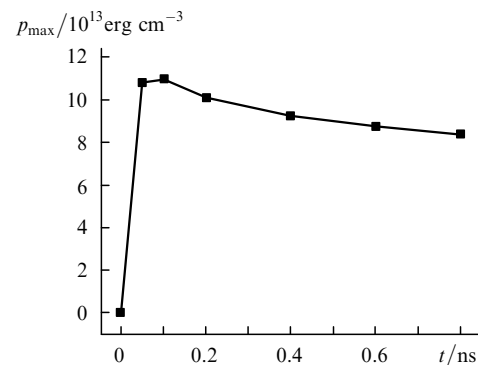

Figure 10. Time dependence of the maximum pressure p_{max} on the shock-wave front.

The radiation intensity over the beam cross section was constant. Radiation was incident on an aluminium layer with the initial thickness of 60 μm.

Thus, except for the initial interaction stage, pressure decreases during the evaporation of the external layers of the target and propagation of the shock wave deep in a material. Therefore, the velocity V_{sw} also changes, and we can deal only with average velocities obtained in experiments with step target surfaces and in corresponding numerical calculations.

4. Discussion of results and conclusions

Numerical calculations allow us to take into account a variety of physical phenomena realised in experiments. Relations (1) – (3) between physical parameters obtained from numerical calculations are approximate and valid only in a certain range of parameters for the corresponding irradiation geometry of a target. Consider, for example, the influence of the pulse duration on plasma parameters. It was pointed out in [16] that the ablation pressure decreased during target heating even for the constant laser radiation intensity. The consideration of distributed absorption in the plasma changes the dependence of the ablation pressure on the radiation intensity, wavelength, and 'corona' size compared to this dependence in the case of 'delta-like' absorption, which was used in earlier models [17 – 19]. Note that the dependences of the ablation pressure and the evaporation rate of materials on laser radiation parameters were obtained in the papers of Russian researchers by using the model of a spherical stationary corona. Attempts to obtain the stationary solution in a planar case have failed, while the nonstationary model of an isothermal corona contains the parameter $L = C_s t$. The focal spot diameter d_f in experiments with the PALS laser was ∼ 400 μm, while the laser pulse duration was 0.8 ns, i.e. $L \leqslant d_f$. For low laser radiation powers and intensities ∼ $10^{14} - 10^{15}$ W cm^{-2}, the focal spot diameter can be smaller than L. Therefore, the dependence of pressure on laser radiation parameters should be described by talking into account the real geometry of the problem.

The relations obtained above are modified if the nonuniform irradiation of a target is taken into account. To verify it, we performed a number of two-dimensional calculations with the Gaussian radiation intensity distribution in the beam cross section, i.e. $I(r, t) = I_1(t)I_2(r)$ and $I_2(r) \sim \exp[-(r/R_f)^2]$. Calculations were performed for radiation wavelengths 0.438 and 1.314 μm. The laser pulse shape was described, as earlier, by an isosceles triangle and its duration was 0.8 ns. The pulse energy and focal spot radius were varied so that the ratio E_{las}/R_f^2 was preserved (i.e. the radiation intensity averaged over the focal spot was preserved). The transverse size of the calculation region was $R_0 = 4R_f$. Table 4 presents maximum pressures on the beam axis at the instant $t = 0.4$ ns. Pressure in two-dimensional calculations in the case of the Gaussian intensity distribution along the beam radius only asymptotically tends to the values obtained in the case of the rectangular intensity distribution (Fig. 11).

Note that for the maximum intensity $I_{max} = 2E_{las} \times (\tau_{las}\pi R_f^2)^{-1} = 1.99 \times 10^{14}$ W cm^{-2} averaged over the focal spot, pressure on the shock-wave front is lower than that in one-dimensional calculations (due to transverse propagation of the shock wave), the smaller the focal spot radius, the

Table 4.

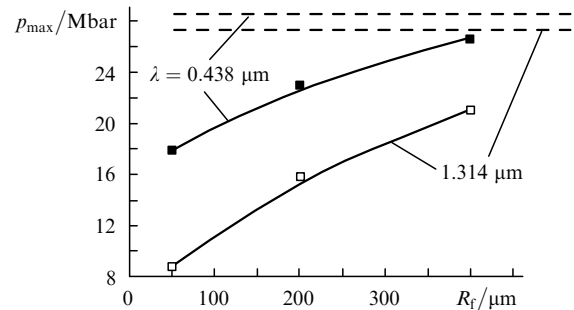| E_{las}/J	$R_f/\mu m$	$p_{max}/Mbar$	
		$\lambda = 0.438$ μm	$\lambda = 1.314$ μm
6.25	50	18	8.6
100	200	23	15.8
400	400	26.6	21

Figure 11. Dependences of maximum pressures on the *z* axis on the focal spot radius for $t = 0.4$ ns obtained in two-dimensional calculations for laser wavelengths 0.438 and 1.314 μm and $E_{las}/R_f^2 = $ const. The dashed straight lines are asymptotic values obtained for the rectangular distribution of the laser radiation intensity.

more pronounced this effect. In addition, for $\lambda = 1.314$ μm the discrepancy between the results of calculations and the one-dimensional similarity relation increases[*].

Figure 12 shows the dependences of the plasma density on the distance along the target surface and contours of the plasma density in plumes produced upon irradiation of a flat aluminium target by a Gaussian laser beam for $R_f = 50$ μm at wavelengths 0.438 and 1.314 μm. One can see that the density distributions in the plasma plume are substantially non-one-dimensional, and for = 1.314 μm the distance from the surface with the critical density to the evaporation boundary noticeably exceeds the focal spot radius R_f. Therefore, the influence of the shock-wave propagation in the direction perpendicular to the laser beam axis will be more considerable.

In conclusion, we formulate briefly the main results of the paper:

(i) The results of calculations performed by using the Atlant program are in good agreement, taking into account corrections for losses, with experimental data obtained on the PALS setup;

(ii) the shock-wave velocities, pressures, and densities behind the shock-wave front calculated by using the QEOS and ZRI models are close to each other;

(iii) upon irradiation of plane targets, dependences of the pressure and velocity of the shock wave propagating from the target on laser radiation parameters (the laser wavelength was 0.35 – 1.3 μm and the laser energy was 100 – 400 J) considerably differ from similarity relations obtained by assuming the stationary spherical plasma expansion;

(iv) pressure in a compressed material in experiments with plane targets also depends on the focal spot radius (or on the pulse energy at the fixed radiation intensity), which

---

[*] Note that the wavelength dependence of the ablation pressure p_a in the model of a quasi-stationary spherical corona has the form $p_a \sim \lambda^{-0.7}$ in the case of 'delta-like' absorption of laser radiation and is somewhat weaker in the case of the inverse braking absorption mechanism [19]. In the case under study, we have $p_a \sim \lambda^{-0.056}$.
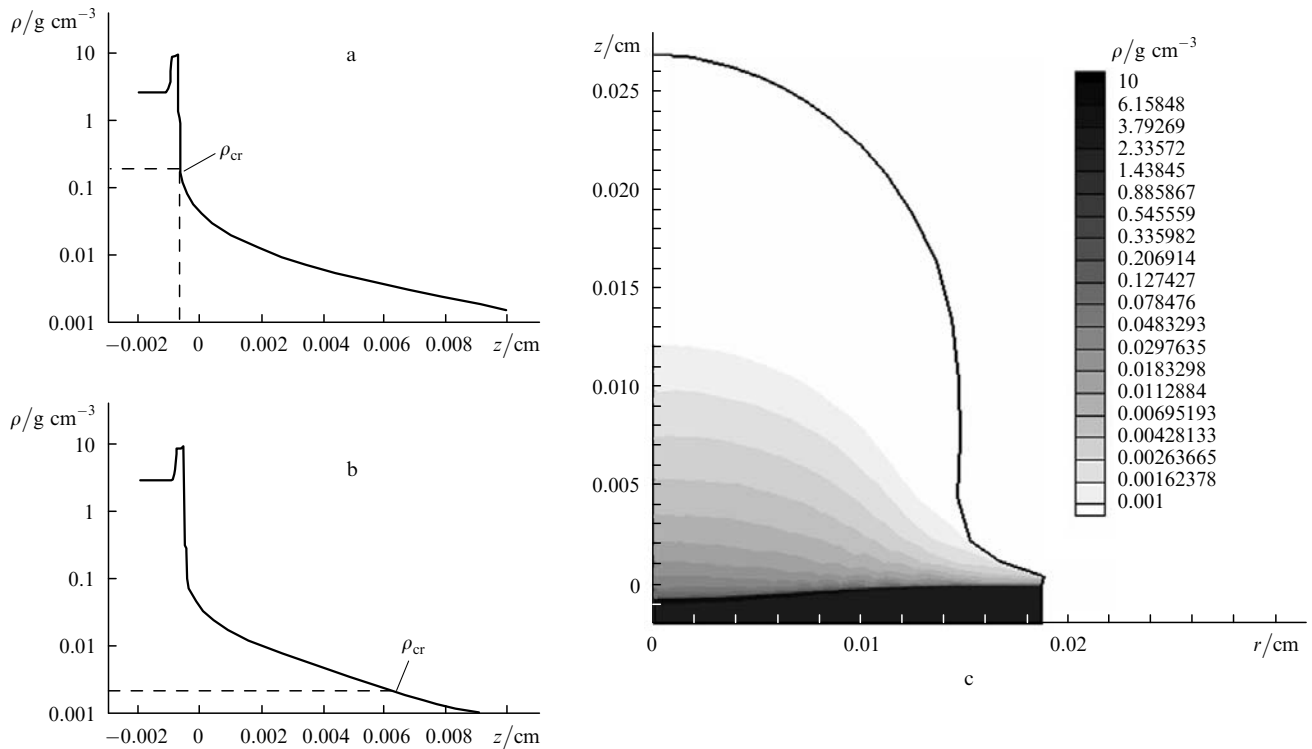
Figure 12. Two-dimensional numerical calculations at the instant $t = 0.4$ ns: distributions of density ρ along the z axis upon exposure to laser radiation at 0.438 μm (a) and 1.314 μm (b) and two-dimensional plasma density profiles at $\lambda = 0.438$ μm (c) (ρ_{cr} is the critical density).

explains the discrepancy between experimental similarity relations obtain on different setups at different laser radiation energies;

(v) when the absorbed energy density is fixed, pressure at the shock-wave front weakly depends on the laser radiation wavelength in the one-dimensional planar geometry considered. This dependence considerably differs from the corresponding dependence obtained upon spherical irradiation of the target. It would be expedient to perform a new series of experiments with a step target by using irradiation at wavelengths 1.314 and 0.657 μm (the first and second harmonics). This will allow studying the influence of radiation reflection and energy transfer by 'hot' electrons on the formation of the ablation pressure and on the hydrodynamic efficiency of the target (the ratio of the kinetic energy of a nonevaporated target material to the absorbed laser energy). The Atlant software package provides the accounting of these processes [20].

References

1. Afanas'ev Yu.V., Gamalii E.G., Krokhin O.N., Rozanov V.B. *Zh. Eksp. Teor. Fiz.*, **71**, 594 (1976).
2. Fabbro R. et al. *Phys. Rev. A.*, **26**, 2289 (1982); Fabbro R., Max C., Fabre E. *Phys. Fluids*, **28**, 2585 (1985).
3. Mora P. *Phys. Fluids*, **25**, 1051 (1982).
4. Afanas'ev Yu.V., Gamalii E.G., Demchenko N.N., Rozanov V.B. *Trudy FIAN*, **134**, 43 (1982).
5. Basov N.G. (Ed.) *Diagnostika plotnoi plazmy* (Diagnostics of Dense Plasmas) (Moscow: Nauka, 1989).
6. Dahmani F., Kerdjia T. *Phys. Rev. A*, **44** (4), 267 (1991).
7. Vovchenko V.V., Krasyuk I.K., Pashinin P.P., Semenov A.Yu. *Dokl. Ross. Akad. Nauk*, **338**, 322 (1994).
8. Lindl J. *Phys. Plasmas*, **2**, 3933 (1995).
9. Batani D., Stabile H., Ravasio H., et al. *Phys. Revi. E*, **68**, 067403 (2003).
10. Lebo I.G., Tishkin V.F. *Issledovanie gidrodinamicheskoi neustoichivosti v zadachakh lazernogo termoyadernogo sinteza* (Study of the Hydrodynamic Instability in Nuclear Fusion Problems) (Moscow: Fizmatlit, 2006).
11. More R.M. et al. *Phys. Fluids*, **31**, 3059 (1988).
12. Afanas'ev Yu.V., Gamalii E.G., Rozanov V.B. *Trudy FIAN*, **134**, 10 (1982).
13. Zel'dovich Ya.B., Raizer M.P. *Physics of Shock Waves and High-Temperature Hydrodynamic Phenomena* (New York: Academic Press, 1966; Moscow: Nauka, 1966).
14. Friedland L., Bernstein I.B. *Phys. Rev. A*, **21** (2), 666 (1980).
15. Iskakov A.B., Lebo I.G., Popov I.P., Rozanov V.B., Tishkin V.F. *Kratk. Soobshch. Fiz. FIAN*, (1-2), 28 (1997).
16. Caruso A., Gratton R. *Plasma Phys.*, **10**, 867 (1968).
17. Gus'kov S.Yu., Zverev V.V., Rozanov V.B. *Kvantovaya Elektron.*, **10**, 802 (1983) [*Sov. J. Quantum Electron.*, **13**, 498 (1983)].
18. Meyer B., Thiell G. *Phys. Fluids*, **27**, 302 (1984).
19. Limpoukh I., Lebo I.G., Rozanov V.B. *Kratk. Soobshch. Fiz. FIAN*, (11), 23 (1987).
20. Lebo I.G., Demchenko N.N., Iskakov A.B., et al. *Laser Part. Beams*, **22**, 267 (2004).